Received: 12 August 2024 | Revised: 18 April 2025 | Accepted: 19 April 2025

DOI: 10.1002/mp.17867

RESEARCH ARTICLE

MEDICAL PHYSICS

Generation of synthetic CT from MRI for MRI-based attenuation correction of brain PET images using radiomics and machine learning

Amin Hoseinipourasl[1,2] | **Gholam-Ali Hossein-Zadeh**[3] | **Peyman Sheikhzadeh**[4] | **Hossein Arabalibeik**[5] | **Shaghayegh Karimi Alavijeh**[2] | **Habib Zaidi**[6,7,8,9] | **Mohammad Reza Ay**[1,2]

[1]Research Center for Molecular and Cellular Imaging (RCMCI), Advanced Medical Technologies and Equipment Institute (AMTEI), Tehran University of Medical Sciences (TUMS), Tehran, Iran

[2]Department of Medical Physics and Biomedical Engineering, Tehran University of Medical Sciences, Tehran, Iran

[3]School of Electrical and Computer Engineering, College of Engineering, University of Tehran, Tehran, Iran

[4]Nuclear Medicine Department, IKHC, Faculty of Medicine, Tehran University of Medical Science, Tehran, Iran

[5]Research Center for Biomedical Technologies and Robotics, Tehran University of Medical Sciences, IK Hospital Complex, Tehran, Iran

[6]Division of Nuclear Medicine & Molecular Imaging, Geneva University Hospital, Geneva, Switzerland

[7]Department of Nuclear Medicine and Molecular Imaging, University of Groningen, University Medical Center Groningen, Groningen, Netherlands

[8]Department of Nuclear Medicine, University of Southern Denmark, Odense, Denmark

[9]University Research and Innovation Center, Óbuda University, Budapest, Hungary

Correspondence
Habib Zaidi, Geneva University Hospital, Radiology and Medical Informatics, Division of Nuclear Medicine and Molecular Imaging, Geneva CH-1211, Switzerland.
Email: habib.zaidi@hug.ch

Mohammad Reza Ay, Department of Medical Physics and Biomedical Engineering, School of Medicine, Tehran University of Medical Sciences, Tehran, Iran.
Email: mohammadreza_ay@sina.tums.ac.ir

Funding information
Tehran University of Medical Sciences, Grant/Award Number: 57558; Swiss National Science Foundation, Grant/Award Number: SNSF 320030_231742; National Brain Mapping Laboratory (NBML)

Abstract

Background: Accurate quantitative PET imaging in neurological studies requires proper attenuation correction. MRI-guided attenuation correction in PET/MRI remains challenging owing to the lack of direct relationship between MRI intensities and linear attenuation coefficients.

Purpose: This study aims at generating accurate patient-specific synthetic CT volumes, attenuation maps, and attenuation correction factor (ACF) sinograms with continuous values utilizing a combination of machine learning algorithms, image processing techniques, and voxel-based radiomics feature extraction approaches.

Methods: Brain MR images of ten healthy volunteers were acquired using IR-pointwise encoding time reduction with radial acquisition (IR-PETRA) and VIBE-Dixon techniques. synthetic CT (SCT) images, attenuation maps, and attenuation correction factors (ACFs) were generated using the LightGBM, a fast and accurate machine learning algorithm, from the radiomics-based and image processing-based feature maps of MR images. Additionally, ultra-low-dose CT images of the same volunteers were acquired and served as the standard of reference for evaluation. The SCT images, attenuation maps, and ACF sinograms were assessed using qualitative and quantitative evaluation metrics and compared against their corresponding reference images, attenuation maps, and ACF sinograms.

Results: The voxel-wise and volume-wise comparison between synthetic and reference CT images yielded an average mean absolute error of 60.75 ± 8.8 HUs, an average structural similarity index of 0.88 ± 0.02, and an average peak signal-to-noise ratio of 32.83 ± 2.74 dB. Additionally, we compared MRI-based

attenuation maps and ACF sinograms with their CT-based counterparts, revealing average normalized mean absolute errors of 1.48% and 1.33%, respectively.
Conclusion: Quantitative assessments indicated higher correlations and similarities between LightGBM-synthesized CT and Reference CT images. Moreover, the cross-validation results showed the possibility of producing accurate SCT images, MRI-based attenuation maps, and ACF sinograms. This might spur the implementation of MRI-based attenuation correction on PET/MRI and dedicated brain PET scanners with lower computational time using CPU-based processors.

KEYWORDS
attenuation correction, machine learning, PET/MRI, radiomics, synthetic CT

1 | INTRODUCTION

Reaching the full potential of quantitative PET imaging in neurological studies requires accurate correction of physical degrading factors including photon attenuation. Attenuation correction of PET data requires patient-specific attenuation map containing the distribution of attenuation coefficients of tissues inside the body.[1] PET/CT scanners commonly use energy mapping techniques, such as piecewise linear scaling to obtain the required attenuation map directly from CT images.[2] Hybrid PET/MRI systems offer several advantages over PET/CT systems.[3] Nevertheless, attenuation correction in PET/MRI is challenging owing to the MR signal's dependence on tissues' proton density and relaxation times instead of electron density.[4] Furthermore, in conventional MR images, cortical bone and air voxels exhibit similar appearances despite their different attenuation properties. Cortical bone tissues have very low proton density (only 20% water) and a very short T2 relaxation time (only 390 µs at 3 Tesla), making it difficult to differentiate them from air voxels.[5] Ignoring bone voxels during PET attenuation correction can cause significant errors of up to 25% in the head region and 17%–23% in whole-body imaging.[6,7]

Several approaches have been proposed to generate PET attenuation maps from MRI.[8] The two primary approaches are atlas-based and segmentation-based methods. Atlas-based methods rely on normal anatomy and cannot consider anatomical variations. On the other hand, segmentation-based approaches use patient-specific segmented brain MR images, but they are prone to tissue classification errors, especially in air/bone regions. Most recent MRAC techniques use artificial intelligence techniques to identify patterns and relations between input MR images and output CT images.[9–13] They create synthetic CT (SCT) images or attenuation maps for PET attenuation correction based on input MR images.[14] Additionally, continuous Hounsfield Unit (HU) values in SCT images and continuous linear attenuation coefficient (LAC) values in attenuation maps are essential for proper attenuation correction in PET/MRI and dedicated brain PET only scanners.[15] The use of discrete values, especially in bone voxels, can negatively impact the performance of attenuation correction methods. Despite numerous studies, MRAC still remains a challenge in PET/MRI systems.[16–18]

Machine learning models rely significantly on feature engineering to identify and select relevant features. In contrast, deep learning models employ deep neural networks to automatically extract features, thereby diminishing the need for manual intervention. While machine learning typically exhibits superior performance with smaller datasets and can yield robust outcomes when utilizing handcrafted features, deep learning necessitates substantial amounts of data for effective training and demonstrates enhancements with larger datasets. Furthermore, machine learning algorithms generally afford greater interpretability, thereby facilitating the comprehension and optimization of processes. Conversely, deep learning is often marked by lower interpretability, complicating optimization processes. Moreover, machine learning is particularly well-adapted for traditional computing systems, utilizing the CPU for rapid processing. Conversely, deep learning depends on sophisticated infrastructure, frequently employing GPUs, and typically requires more extended training periods, occasionally spanning several days.[19,20]

Radiomics techniques rely on the extraction of complex features from medical images, enabling models to identify intricate patterns and voxel relationships that traditional assessment methods may overlook.[21,22] These features provide objective, quantitative data about various anatomical structures, reducing human bias and variability in interpretations. Consequently, this detailed voxel-based information facilitates the training of robust AI models with improved accuracy. Integrating radiomics-based features, image processing techniques, advanced machine learning algorithms, and automated hyperparameter tuning frameworks enables the development of artificial intelligence models that convert MR images into synthetic CT images.

In this study, we proposed a novel approach that integrates, for the first time, advanced machine learning algorithms, voxel-based radiomics feature extraction methods, and image processing techniques to effectively generate accurate SCT images, MRI-based attenuation maps, and ACF sinograms from MR images without using a GPU or advanced processors. This approach is suitable for MRI-based attenuation correction on PET/MRI and dedicated brain PET scanners. Additionally, we obtained ultra-low-dose head CT images to validate our approach and compare them with synthetic images. The preprocessing and training stages were performed on simple CPU-based processors with lower computational time.

2 | MATERIALS AND METHODS

2.1 | Data acquisition

Recent advances in MRI allow capturing signals from short-T2 tissues, such as bone voxels using zero echo time (ZTE) imaging techniques.[23] However, without performing k-space gap-filling in ZTE techniques, the reconstruction of the acquired data can lead to low spatial frequency artifacts.[24] PETRA sequence fills the ZTE central gap region using single-point imaging (SPI) with decreased gradient strength and constant encoding time.[25]

Compared to UTE, PETRA exhibits a significant increase in SNR for T2 values of 100 µs, 250 µs, and 750 µs, with improvements of 53%, 19%, and 6%, respectively. Additionally, PETRA demonstrates 70% higher SNR for cortical bone and 36% higher bone/air CNR than UTE. PETRA offers improved image resolution for short T2 tissues, such as bone, lower acoustic noise levels, and reduced susceptibility artifacts compared to UTE.[26] The modified PETRA sequence, IR-PETRA, begins with an inversion pulse, resulting in T1-weighted contrast. In IR-PETRA, the Cartesian component of k-space is sampled immediately following the first inversion pulse, while the radial component is projected after the second and subsequent inversion pulses.[27]

The proposed CT and MR imaging protocols were approved by the Ethical Committee of Tehran University of Medical Sciences (Ethic license number 1401.037). Ten healthy volunteers (five male and five female) participated in this study after providing written consent. In addition to IR-PETRA, all volunteers underwent CAIPIRINHA-accelerated T1 VIBE DIXON MR data acquisition. This sequence generates in-phase and out-of-phase images using two different echo times. Additionally, mathematical computations can be employed to produce fat and water images. All magnetic resonance scans were conducted on a 3T MR scanner (MAGNETOM Prisma, Siemens, Erlangen, Germany) and a 20-channel head/neck coil. To assess the performance of the MRI to SCT conversion algorithm, we acquired ultra-low-dose helical head CT images from the same volunteers using an ULD-CT protocol[28] on the CT module of the Discovery IQ PET/CT scanner (GE Healthcare Technologies, WI, USA). The total effective dose of the ULD-CT protocol was about 0.5% of the standard head CT scan. All CT and MR imaging parameters are summarized in Table 1.

2.2 | Data processing

We performed correction of bias magnetic field using the N4ITK algorithm[29] with a BSpline grid resolution of (1,1,1), a convergence threshold of 0.0001, a BSpline order of 3, and a shrink factor of 4. Furthermore, we employed a non-local transform domain filtering algorithm, referred to as the 4D block-matching technique[30] to denoise ULD-CT images while maintaining their details and essential characteristics. Due to a lower photon flux, ULD-CT images have higher noise levels. In the following, we registered the 3D MR and CT images using the BRAINS module of the Insight Toolkit in 3D Slicer software version 5.2.1 (http://www.slicer.org) with an affine transformation, linear interpolation mode, B-Spline grid size (14,10,12), and the mattes mutual information (MMI) registration cost metric.

2.3 | Generating SCT images from MRI

The 3D voxel-based radiomics feature maps were extracted from MR images using the PyRadiomics library.[31] These first-order and second-order radiomics feature maps were transformed into feature vectors the same size as the target label vectors.[32] In addition to radiomics feature maps, several image processing-based features were extracted from MR images, including a logarithmic map, gamma-adjusted image, Gaussian and median filtered images, and logarithmic exponential map. Once feature extraction was completed, we applied different feature selection techniques to select the most relevant and essential features to use as machine learning model inputs. Feature selection is an essential step in machine learning model creation, focusing on identifying the most relevant features from the dataset. It enhances model performance, reduces overfitting, and improves model interpretability. Common techniques include Filter methods, which use statistical measures to assess feature relevance; Wrapper methods, which evaluate subsets of features based on their impact on model performance; and embedded methods, which select features based on their contribution throughout model training. We extract radiomics-based and image-processing-based feature maps from IR-PETRA and VIBE-DIXON MR images. Afterward, we applied feature selection methods to identify 15 feature maps that were the most relevant for training our

TABLE 1 CT and MR imaging protocols and acquisition parameters.

CT imaging		MR imaging		
Parameter	**ULD-CT**	**Parameter**	**IR-PETRA**	**VIBE-DIXON**
Protocol	Helical head	Orientation	Transversal	Transversal
Matrix size	512 × 512	Dimension	3D	3D
Voxel size (mm)	0.5 × 0.5 × 2.5	TE(s) (ms)	0.07	2.46–3.69
kVp	80	TR(s) (ms)	3.32–2250	6.44
mA	10	TI(s) (ms)	1300–900	-
Rotation time (s)	0.5	Flip angle (°)	6	12
Slice numbers	~70:80	Bandwidth (Hz/Px)	401	650–320
		Voxel size (mm)	0.9 × 0.9 × 0.9	0.7 × 0.7 × 2.0
		FOV (mm2)	300 × 300	250 × 250
		Acquisition time (min)	5:57	3:33
		No. of Radial views	60000	-
		Slice per slab	320	112
		Averages	1	1

Abbreviation: IR-PETRA, IR-pointwise encoding time reduction with radial acquisition

model and generating SCT images. Most of the selected features are first-order radiomics-based features.[33,34] To achieve more robust results, we employed all three feature selection methods. The feature maps that exhibited the highest frequency across these three methods were subsequently selected for training the ML model.

Ensemble and hybrid machine learning algorithms combine multiple learners to improve model performance and reduce bias and variance. Boosting is one of the most popular ensemble techniques, where weak learners are trained sequentially to create a robust model. Gradient boosting machine (GBM) is a tree-based boosting algorithm that utilizes the gradient descent optimization algorithm to minimize the loss function and iteratively enhance model performance. Extreme gradient boosting (XGBoost) is an advanced version of GBM that can handle overfitting, missing values, and best split finding with excellent efficiency.[35]

Light gradient boosting machine (LightGBM) is a robust open-source gradient-boosting algorithm developed by Microsoft in 2017. It is an improved version of XGBoost, designed to handle computational challenges associated with vast high-dimensional datasets.[36] LightGBM has several advanced features, such as exclusive feature bundling (EFB) that helps reducing the dimensionality of the data, gradient-based one-side sampling (GOSS) that focuses on the large gradient (error) training data points, Leaf-wise tree growth that reduces memory usage during the training, parallel processing and distributed computing support that enable fast handling of large datasets, and advanced regularization techniques like Dropouts meet Multiple Additive Regression Trees (DART) that overcome model overspecialization.[37]

We utilized the LGBMRegressor module from the LightGBM library, employing DART boosting and GOSS data sampling to enhance model performance and generate accurate SCT images. As illustrated in Figure 1, we organized the selected features from MR images into a data frame, which served as the input for the machine learning model during the training process. This approach produces synthetic CT volumes as the output of the LGBMRegressor model, with continuous HU values.

In addition, we utilized the Optuna library, an automatic hyperparameter optimization and tuning framework, to optimize LightGBM's. We employed a 10-fold leave-one-out cross-validation (LOOCV) technique to validate the model's efficacy on previously unseen data. This involved tuning LightGBM hyperparameters using one validation fold, training LightGBM using nine training folds, and predicting SCT from a single test fold. This procedure is repeated ten times to generate synthetic CT for all ten volunteers. Our proposed approach to generate SCT images and their corresponding leave-one-out cross-validation technique is summarized in Figure 1. This figure reveals that the study involves several steps: (1) Acquiring VIBE-DIXON and IR-PETRA MR images and ULD-CT images from ten healthy subjects. (2) Registering the MR and CT images. (3) Extracting radiomics and image processing feature maps from MR images. (4) Applying feature selection techniques to these maps. (5) Generating input data frames in Python environment. (6) Conducting 10-fold leave-one-out cross-validation while optimizing LightGBM with Optuna. (7) Training LightGBM on data from nine subjects to predict an SCT image for a test subject. (8) Comparing CT and SCT images pairwise.

The algorithm employed in this study used 64-bit Python version 3.9.10 as its internal software, operating on an Intel Core i7 CPU 6700HQ @ 2.60 GHz × 8 with 16 GB of RAM. We calculated the computational time involving feature extraction, model training, and model prediction processes to facilitate comparative analysis of our model with previously reported models.

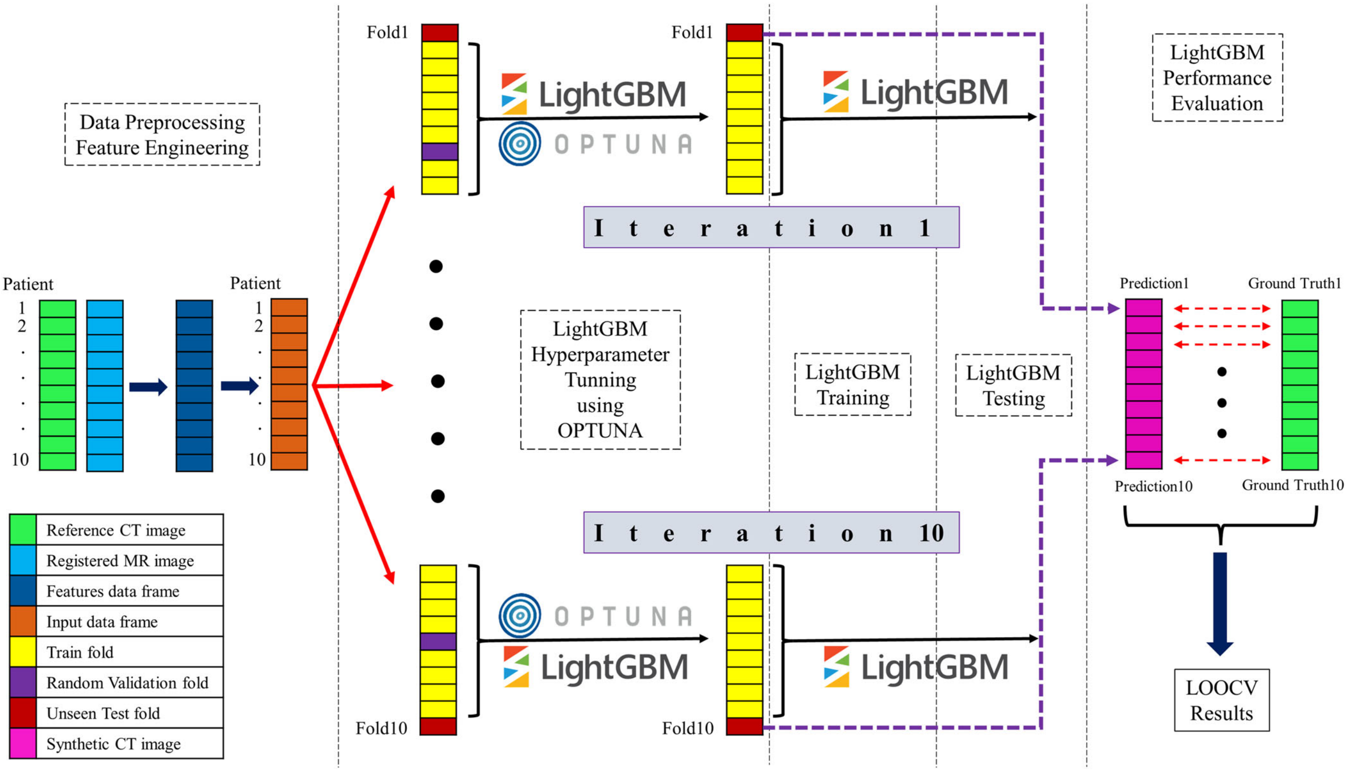

FIGURE 1 Schematic overview of the proposed ML-based SCT generation approach.

2.4 | Generating MR-based and CT-based attenuation maps and ACF sinograms

The trilinear conversion of 80 kVp CT HU values to 511 KeV PET LACs (cm^{-1}) was adopted from Abella et al.[38] as given in Equation 1. We used this scaling method to create attenuation maps and obtain PET LACs from CT values. In the following, we applied the Radon transform to the attenuation maps to generate corresponding ACF sinograms.

$$\begin{aligned} &\mathrm{LAC} = 9.30\times10^{-5}\times\mathrm{HU} + 0.093 : -1000 < HU < 0\\ &\mathrm{LAC} = 3.28\times10^{-5}\times\mathrm{HU} + 0.093 : 0 < HU < 1000\\ &\mathrm{LAC} = 4.10\times10^{-6}\times\mathrm{HU} + 0.122 : 1000 < HU < 30000 \end{aligned} \tag{1}$$

2.5 | Evaluation metrics

We conducted a thorough analysis of SCT images, MRI-based attenuation maps, and ACF sinograms using various evaluation metrics. Our evaluation metrics consisted of voxel-wise assessments including the mean absolute error (MAE) and normalized mean absolute error (NMAE), as well as volume-wise assessments including relative volume difference (RVD). To assess image quality, we utilized metrics, such as the structural similarity index measure (SSIM), peak signal-to-noise ratio (PSNR), and universal quality index (UQI). Additionally, we employed the Pearson correlation coefficient (PCC) to determine the linear correlation between predicted and reference images.

$$\mathrm{NMAE}(P,G) = \frac{\mathrm{MAE}}{\mathrm{DR}} = \frac{1}{\mathrm{DR}}\left(\frac{1}{xyz}\sum_{i=0}^{x-1}\sum_{j=0}^{y-1}\sum_{k=0}^{z-1}\left|G(i,j,k) - P(i,j,k)\right|\right)$$

$$\mathrm{RVD}(P,G)\,\% = \frac{\sum\sum\sum P(i,j,k) - \sum\sum\sum G(i,j,k)}{\sum\sum\sum G(i,j,k)}$$

$$\mathrm{SSIM}(P,G) = \frac{(2\mu_G\mu_P + C_1)(2\sigma_{GP} + C_2)}{\left(\mu_G^2 + \mu_P^2 + C_1\right)\left(\sigma_G^2 + \sigma_P^2 + C_2\right)}$$

$$\mathrm{PSNR}(P,G) = 10\log_{10}\left(\frac{G_{max}^2}{\mathrm{MSE}(G,P)}\right)$$

$$\mathrm{UQI}(P,G) = \frac{4\sigma_{GP}GP}{\left(\sigma_G^2 + \sigma_P^2\right)\left[(G)^2 + (P)^2\right]}$$

$$\mathrm{PCC}(P,G) = \frac{\sum(G_i - G)(P_i - P)}{\sqrt{\sum(G_i - G)^2\sum(P_i - P)^2}}$$

where G and P represent corresponding pixel values in the reference and predicted images, and x, y, and z represent the image dimensions. DR is the dynamic range of the image pixel values, whereas G_{max} is the maximum pixel value of the reference CT image. $C_1 = (k_1 DR)^2$, $C_2 = (k_2 DR)^2$, $k_1 = 0.01$, and $k_2 = 0.03$ by default.

Additionally, we compared segmented CT images with segmented SCT images. Our analysis involved the calculation of various metrics, including the Dice similarity coefficient (DSC), accuracy, area under receiver operating characteristic curve (AUROC), precision, recall (sensitivity), and specificity (selectivity). Specific thresholds were applied to CT and SCT images to segment air, bone, and soft tissue. Values greater than 300 HU were set to identify bone, while values less than −300 HU were mapped to air. Any values falling outside these ranges were labeled as soft tissue. This classification metric was calculated separately for each tissue class, including bone, air, and soft tissue. Moreover, we utilized histogram-wise and slice-wise techniques to further evaluate the generated synthetic CT images, attenuation maps, and ACF sinograms.

3 | RESULTS

The LightGBM model was trained and evaluated using 10-fold leave-one-out cross-validation. The presented metrics were computed across the entire dataset. Figure 2 shows the SCT image slices produced by LightGBM and their corresponding IR-PETRA MR and reference CT slices for different volunteer datasets; upon visual inspection by an experienced radiologist, the SCT images generated by LightGBM exhibit lower noise levels, higher signal-to-noise ratios (SNR), and a similar qualitative appearance to the reference CT images.

Figure 3 presents an example of input MR images alongside reference CT images of a randomly selected volunteer dataset. This includes SCT images generated by the LightGBM algorithm and the corresponding binary and multi-class segmented outputs of both CT and SCT datasets. In Figure 4, we present an example of attenuation maps derived from CT and MR images in coronal, sagittal, and axial planes, accompanied by their difference maps and joint histograms of a randomly selected dataset of volunteers. Additionally, this figure illustrates examples of ACF sinograms based on CT and MRI, along with their corresponding difference map and joint histograms. Figures 5 and 6 illustrate representative examples of these histogram-wise and slice-wise evaluations of a random volunteer dataset.

Table 2 summarizes the statistical results, including the mean, standard deviation, minimum, and maximum values for various metrics, such as MAE, NMAE, SSIM, PSNR, UQI, RVD, and PCC. These metrics were calculated between the SCT and reference CT images across the entire dataset. Table 3 outlines the statistical results including the mean, standard deviation, minimum, and maximum values of MAE, NMAE, SSIM, RVD, and PCC metrics for MRI-based attenuation maps

TABLE 2 Summary of the Mean Absolute Error, Normalized Mean Absolute Error, Structural Similarity Index Measure, Peak Signal-to-Noise Ratio, Universal Quality Index, Relative Volume Difference, and Pearson Correlation Coefficient between reference SCT and their corresponding reference CT images using the 10-fold LOOCV technique performed on datasets from 10 volunteers.

Metric	MAE (HU)	NMAE %	SSIM	PSNR (dB)	UQI	RVD %	PCC
avg	60.75	0.78	0.88	32.83	0.85	14.73	0.95
std	8.80	0.23	0.02	2.74	0.02	10.27	0.009
min	46.10	0.47	0.85	28.78	0.82	2.07	0.93
max	74.16	1.10	0.91	36.40	0.89	29.40	0.96

Abbreviations: LOOCV, leave-one-out cross-validation; MAE, mean absolute error; NMAE, normalized mean absolute error; PCC, Pearson correlation coefficient; PSNR, peak signal-to-noise ratio; RVD, relative volume difference; SSIM, structural similarity index measure; UQI, universal quality index.

compared to reference CT-based attenuation maps. It also provides the mean, standard deviation, minimum, and maximum values for the MAE, NMAE, RD, and PCC metrics obtained from MRI-based ACF sinograms compared to reference CT-based ACF sinograms.

Extracting features from a 3D MR image and creating an input data frame takes approximately 30 min. Training the LightGBM model with a 9-fold input requires approximately 60 min, and generating the synthetic CT volume from the test fold takes less than 1 min.

Table 4 displays the evaluation results for the three-class segmented CT and segmented SCT images derived from the dataset of 10 volunteers. The evaluations utilized various metrics, including the Dice similarity coefficient (DSC), accuracy, AUROC, precision, recall (sensitivity), and specificity (selectivity).

4 | DISCUSSION

PET data must undergo a series of corrections to accurately reflect the actual activity distribution. The most crucial correction of PET data is attenuation correction. This correction significantly impacts visual quality and quantitative accuracy, particularly in neurological studies. In hybrid PET/MRI and dedicated brain PET scanners, generating synthetic CT images and attenuation maps from brain MR images is a promising approach for solving the attenuation correction challenge of PET data.[39]

PET attenuation maps can be generated from MRI using different techniques, such as atlas-based, ML-based, and DL-based approaches.[9] However, atlas-based techniques are time-consuming and do not accurately represent patient's anatomical variations. On the other hand, DL-based methods are patient-specific and offer better results, but they require advanced systems with robust processors and GPUs.[40,41] The training phase of DL techniques can take several days, and they need a considerable amount of input data to achieve good results. Deep learning models typically

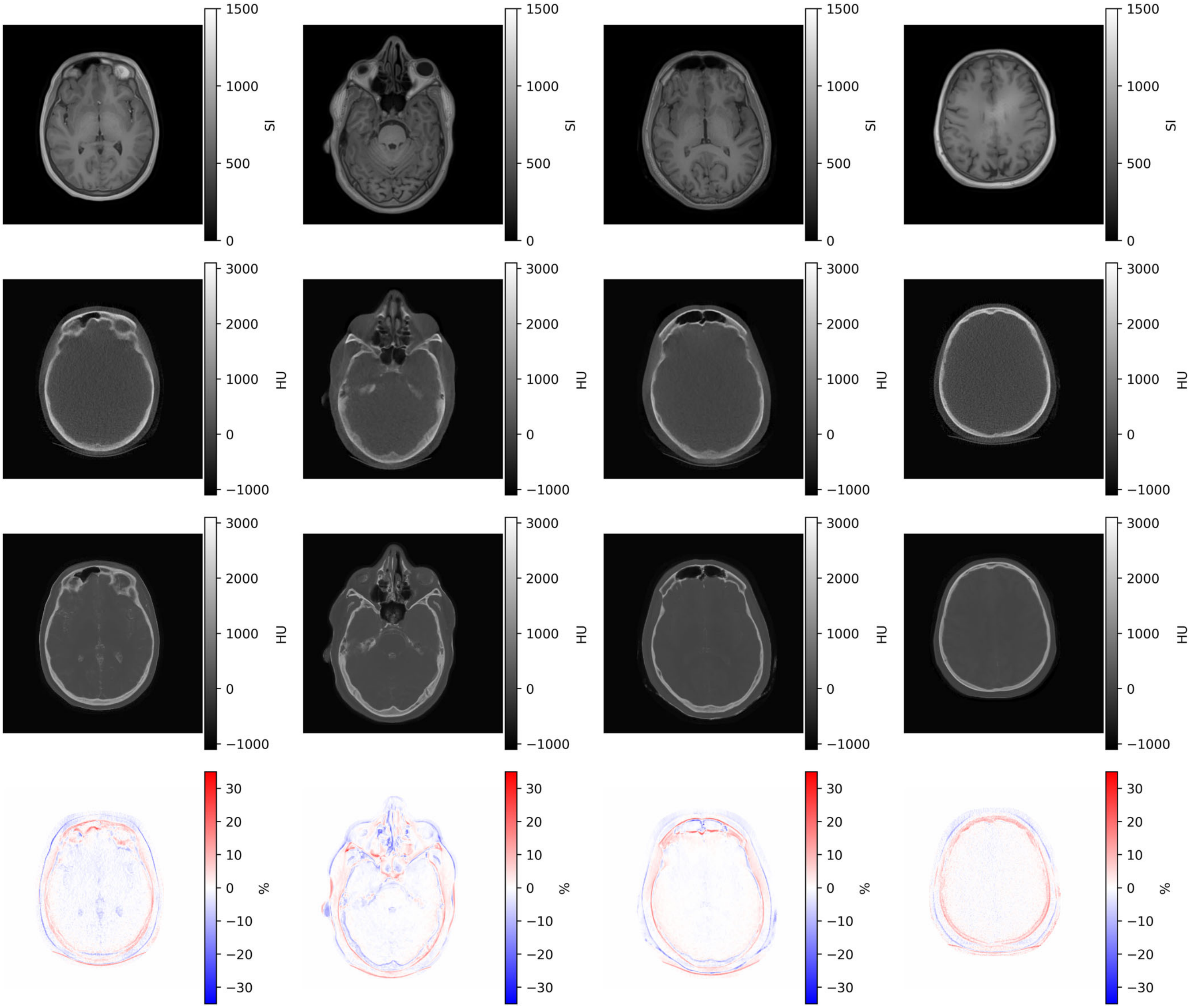

FIGURE 2 Visual representation of input IR-PETRA MR images (first row), reference CT images (second row), generated synthetic CT images (third row), and normalized difference images between reference and synthetic images (fourth row) across various volunteer datasets.

TABLE 3 Quantitative assessment of MRI-based attenuation maps and MRI-based attenuation correction factor (ACF) sinograms compared to reference CT-based maps and sinograms using the 10-fold LOOCV technique performed on datasets from 10 volunteers.

	MRI-based attenuation maps						MRI-based ACF sinograms			
Metric	MAE (cm^{-1})	NMAE %	SSIM	PSNR (dB)	RVD %	PCC	MAE (ACF)	NMAE %	PCC	RVD %
Avg	0.0019	1.48	0.94	28.06	2.09	0.992	0.13	1.33	0.998	9.21
Std	0.0003	0.27	0.013	1.24	1.39	0.002	0.03	0.35	0.001	9.45
Min	0.0013	1.08	0.91	26.35	0.22	0.987	0.09	1.03	0.997	1.72
max	0.0025	2.02	0.96	29.97	5.19	0.995	0.22	2.16	0.999	26.4

Abbreviations: LOOCV, leave-one-out cross-validation; MAE, mean absolute error; NMAE, normalized mean absolute error; PSNR, peak signal-to-noise ratio; SSIM, structural similarity index measure.

require multi-dimensional inputs such as 2D slices or 3D volumes.[42]

Our machine learning approach uses single-dimensional inputs, where each image voxel is considered a sample. Each patient's dataset in this study contains about 20 million voxels, resulting in 200 million samples as the model's total input. We have implemented several fine-tuned regularization

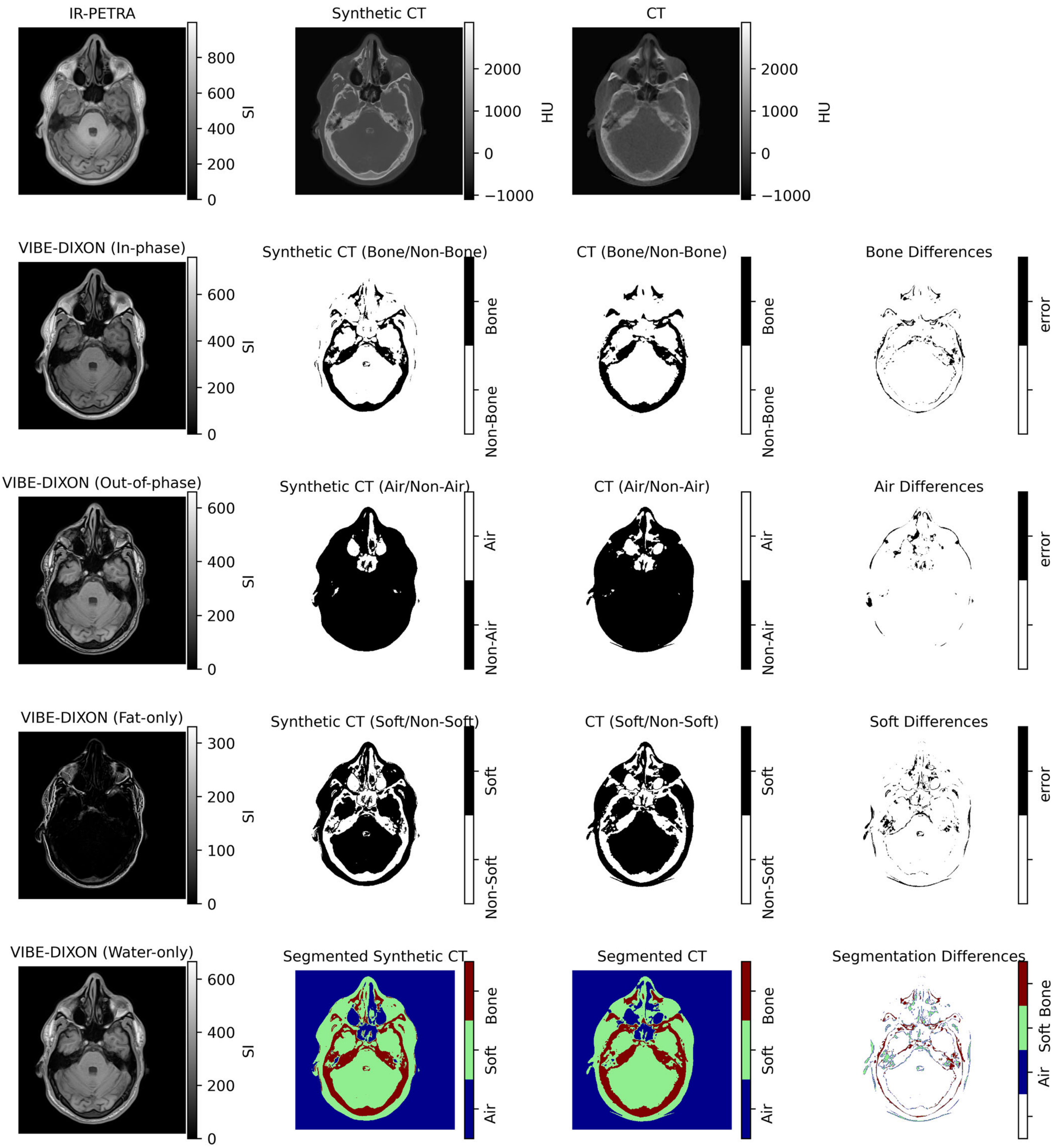

FIGURE 3 Representative illustrations showing input MR image (first column), the synthetic CT image with segmentation results (second column), along with the reference CT image and segmented images (third column). The bias maps between the synthetic and reference images are also displayed (fourth column).

techniques to prevent model over-fitting when working with such vast input data. On the other hand, machine learning approaches are more interpretable than deep learning approaches, and as such, improving and tuning them is much easier.

LightGBM, a machine-learning model known for its high speed and accuracy, is a key component of our work. Its advanced features, like exclusive feature bundling (EFB), Gradient-based One-Side Sampling (GOSS), Leaf-wise tree growth, parallel processing,

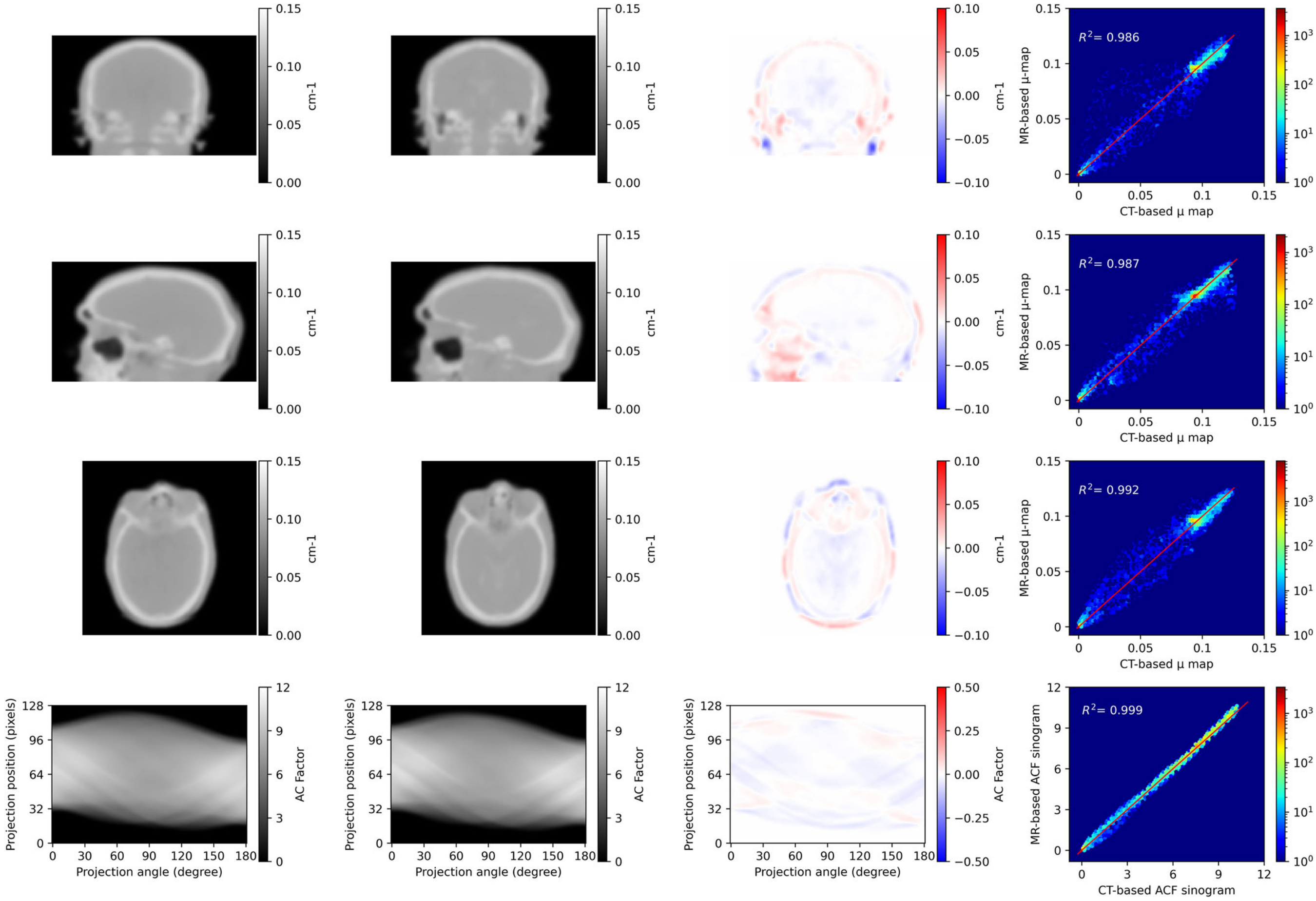

FIGURE 4 The first three rows represent CT-based and MRI-based attenuation maps in coronal, sagittal, and axial views, with their difference map and joint histogram images, respectively. The fourth row shows CT-based and MRI-based ACF sinograms along with their difference map and joint-histogram images. The joint histograms demonstrate significant correlation between CT-based and MRI-based attenuation maps. ACF, attenuation correction factor.

distributed computing support, and advanced regularization techniques, such as DART, ensure its efficiency and consistency.[36] These features enable LightGBM to operate very fast on either CPU(s) or GPU(s) and produce more accurate results with low bias and variance. LightGBM, when properly tuned, can be used as a robust MRI-to-CT conversion model, providing a high level of confidence in the accuracy of our research.

Our proposed model training phase takes approximately 60 min on CPU-based processors. Additionally, it generates a synthetic CT with continuous HUs in less than 1 min. We performed this study using 10 brain datasets, resulting in an average MAE of 60.75 ± 8.8 HUs, representing an improvement over the results reported in the literature.[16,43]

Dovletov et al. utilized T1-weighted MRI datasets from 16 patients to investigate various U-Net and GAN-based deep learning models for synthesizing pseudo-CT images. Their results revealed a MAE of 101 ± 35 HUs, a PSNR of 24.3 ± 1.9 dB, and a structural similarity index metric (SSIM) of 79.6% ± 6.8%.[44] Kläser et al. employed T1 and T2 weighted MRI datasets from 20 patients to implement HighRes3DNet with imitation learning for generating synthetic CT images. Their findings indicated a MAE of 79 ± 3 HUs.[45] Arabi et al. used 3D T1W MPRAGE MR images of 50 patients in conjunction with the Deep Learning Adversarial Semantic Structure (DL-AdvSS) method to produce synthetic CT images.[10] Their findings reported a PSNR of 28 ± 1 dB and SSIM of 87% ± 4%. Boukellouz et al. utilized T1 and T2 weighted MRI datasets from 10 patients and patch-based multi-modal feature extraction in conjunction with Stacked-generalization machine-learning approaches for synthesizing pseudo-CT images.[46] Their findings demonstrated a MAE of 106 ± 18 HUs in the synthesized CT images. This study demonstrated that integrating radiomics, image processing techniques, and machine learning algorithms can produce results that surpass those of many current deep learning methods. Although we recognize that our approach may demonstrate suboptimal performance on specific metrics compared to other studies, it consistently shows comparable or superior results relative to established techniques, even when utilizing a smaller dataset.

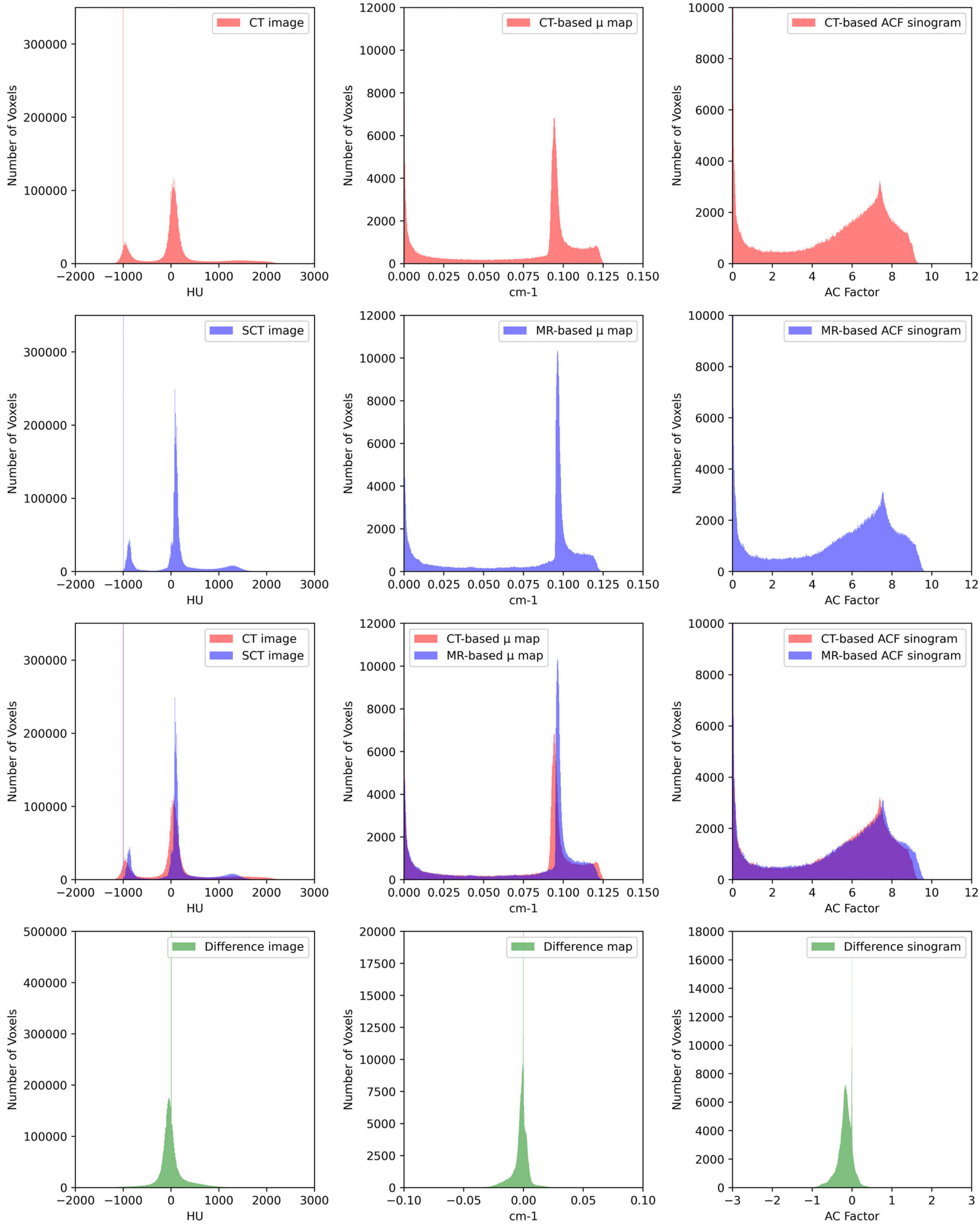

FIGURE 5 Histograms of reference and synthetic CT images, attenuation maps, and ACF sinograms. The third row displays overlapped histograms, indicating a significant similarity between the reference and synthetic ones. Moreover, the histograms of difference or subtracted images, maps, and sinograms in the fourth row demonstrate minimal errors between the reference and synthetic ones. ACF, attenuation correction factor.

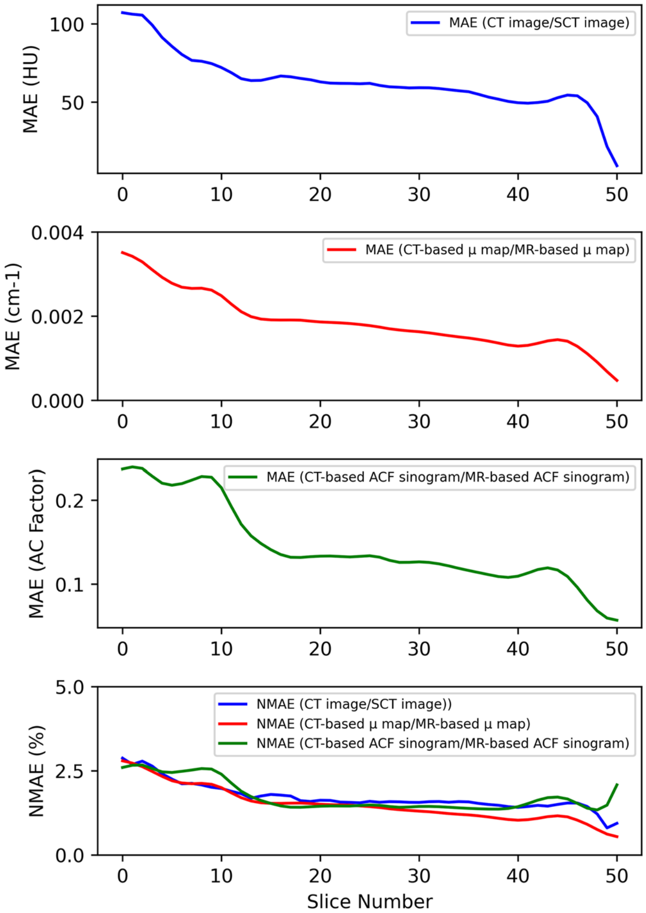

FIGURE 6 The slice-wise MAE and NMAE evaluation show minor errors in the different slices between reference and synthetic CT images, attenuation maps, and ACF sinograms. However, the dental-filling regions have higher MAE values than other head regions. (Note that the slice numbers are arranged from bottom to top within the head region). ACF, attenuation correction factor; MAE, mean absolute error; NMAE, normalized mean absolute error.

The synthetic CT images generated using LightGBM resulted in patient-specific and voxel-specific images with low noise levels, high PSNR, high histogram similarity, and strong correlation to reference CT images. After performing trilinear energy mapping of the synthetic CT images, it was found that MRI-based attenuation maps have an average structural similarity index of 94% $\pm$ 1.3% and an average relative volume difference of 2.09% $\pm$ 1.39% from CT-based attenuation maps. In addition, after performing the Radon transform on attenuation maps, it was discovered that MRI-based ACF sinograms have an average NMAE of 1.33% $\pm$ 0.35% compared to CT-based ACF sinograms. Moreover, MRI-based ACF sinograms demonstrated a high correlation and similarity to their CT-based ACF sinograms.

IR-PETRA sequence helps to achieve bone segmentation accuracy of 97% and an air segmentation accuracy of 98.5% in synthetic CT images. Figure 5

TABLE 4 Comparison of the three-class segmented reference and synthetic CT images results using the 10-fold LOOCV technique performed on datasets from 10 volunteers.

			Bone			
Metric	**Dice**	**Accuracy**	**AUROC**	**Precision**	**Recall**	**Specificity**
avg	0.75	0.97	0.85	0.79	0.72	0.98
std	0.02	0.005	0.03	0.05	0.07	0.006
min	0.71	0.96	0.82	0.65	0.65	0.97
max	0.79	0.98	0.91	0.87	0.84	0.99
			Air			
Metric	**Dice**	**Accuracy**	**AUROC**	**Precision**	**Recall**	**Specificity**
avg	0.989	0.985	0.983	0.992	0.987	0.980
std	0.002	0.002	0.002	0.002	0.002	0.003
min	0.987	0.982	0.980	0.989	0.984	0.975
max	0.993	0.989	0.988	0.996	0.991	0.987
			Soft tissue			
Metric	**Dice**	**Accuracy**	**AUROC**	**Precision**	**Recall**	**Specificity**
avg	0.91	0.96	0.95	0.90	0.93	0.97
std	0.007	0.007	0.01	0.01	0.02	0.007
min	0.90	0.95	0.92	0.88	0.87	0.95
max	0.92	0.97	0.96	0.93	0.95	0.98

Abbreviation: AUROC, area under receiver operating characteristic curve; LOOCV, leave-one-out cross-validation

shows that synthetic and reference images have high histogram similarity and overlapping, especially ACF sinograms. Figure 6 depicts a NMAE of less than 4% in each slice for synthetic CT images, attenuation maps, and ACF sinograms. In summary, the findings suggest that LightGBM has the potential to become a promising approach for generating high-quality and accurate synthetic CT images and MRI-based attenuation maps.

IR-PETRA is an MRI sequence that uses ZTE technology. It is ideal for neurological studies owing to its minimal acoustic noise level, making it a near-silent MR sequence. In addition, by implementing short echo time, radial k-space sampling, and wider receiver bandwidth in IR-PETRA, susceptibility effects can be reduced, especially in air-bone and air-tissue interfaces.[23] These effects can disrupt image processing and machine learning tasks by inducing distortions and signal loss in MR images.

The most significant differences between CT and synthetic CT images were observed around the ear regions and patients' surfaces. These differences could be caused by variations in ear positioning during MRI and CT scans or MR-CT registration errors. Additionally, a significant difference was noted in cases of dental orthodontic brackets, fillings, and implants. Furthermore, we only used MRI of healthy volunteers to generate synthetic CT images in this study since clinical and pathological data sets were not available.

5 | CONCLUSION

This study introduced a novel machine learning and radiomics-based approach for generating synthetic CT images and MRI-based attenuation maps using IR-PETRA and VIBE-DIXON MRI to perform attenuation correction of brain PET data. The proposed algorithm was evaluated using a dataset of ten healthy subjects. The validation results comparing the synthetic and reference CT images, attenuation maps, and ACF sinograms, show high similarity. This study demonstrated the possibility of generating accurate synthetic CT volumes with lower computational time using CPU-based processors and conventional systems.

ACKNOWLEDGMENTS

This study was supported by Tehran University of Medical Sciences under grant number 57558 and the Swiss National Science Foundation under grant SNSF 320030_231742. The authors sincerely acknowledge the National Brain Mapping Laboratory (NBML) in Tehran, Iran, for their invaluable services during data acquisition.

CONFLICT OF INTEREST STATEMENT

The authors declare no conflicts of interest.

REFERENCES

1. Zaidi H, Montandon ML, Meikle S. Strategies for attenuation compensation in neurological PET studies. *Neuroimage*. 2007;34(2):518-541.
2. Ay MR, Sarkar S. Computed tomography based attenuation correction in PET/CT: principles, instrumentation, protocols, artifacts and future trends. *Iran J Nucl Med*. 2007;15(2):1-29.
3. Mannheim JG, Schmid AM, Schwenck J, et al. PET/MRI hybrid systems. *Semin Nucl Med*. 2018;48(4):332-347.
4. Khateri P, Rad HS, Jafari AH, Ay MR. A novel segmentation approach for implementation of MRAC in head PET/MRI employing Short-TE MRI and 2-point Dixon method in a fuzzy C-means framework. *Nucl. Instrum Methods Phys Res A: Accel Spectrom Detect Assoc Equip* 2014;734:171-174.
5. Du J, Carl M, Bydder M, Takahashi A, Chung CB, Bydder GM. Qualitative and quatitative ultrashort echo time (UTE) imaging of cortical bone. *J Magn Reson*. 2010;207(2):304-311.
6. Andersen FL, Ladefoged CN, Beyer T, et al. Combined PET/MR imaging in neurology: mR-based attenuation correction implies a strong spatial bias when ignoring bone. *Neuroimage*. 2014;84:206-216.
7. Arabi H, Rager O, Alem A, Varoquaux A, Becker M, Zaidi H. Clinical assessment of MR-guided 3-class and 4-class attenuation correction in PET/MR. *Mol Imaging Biol*. 2015;17(2):264-276.
8. Chen Y, An H. Attenuation correction of PET/MR imaging. *Magn Reson Imaging Clin N Am*. 2017;25(2):245-255.
9. Mecheter I, Alic L, Abbod M, Amira A, Ji J. MR image-based attenuation correction of brain pet imaging: review of literature on machine learning approaches for segmentation. *J Digit Imaging*. 2020;33(5):1224-1241.
10. Arabi H, Zeng G, Zheng G, Zaidi H. Novel adversarial semantic structure deep learning for MRI-guided attenuation correction in brain PET/MRI. *Eur J Nucl Med Mol Imaging*. 2019;46(13):2746-2759.
11. Arabi H, Dowling JA, Burgos N, et al. Comparative study of algorithms for synthetic CT generation from MRI: consequences for MRI-guided radiation planning in the pelvic region. *Med Phys*. 2018;45(11):5218-5233.
12. Bahrami A, Karimian A, Fatemizadeh E, Arabi H, Zaidi H. A new deep convolutional neural network design with efficient learning capability: application to CT image synthesis from MRI. *Med Phys*. 2020;47(10):5158-5171.
13. Mecheter I, Abbod M, Amira A, Zaidi H. Deep learning with multiresolution handcrafted features for brain MRI segmentation. *Artif Intell Med*. 2022;131:102365.
14. Emami H, Dong M, Nejad-Davarani SP, Glide-Hurst CK. Generating synthetic CTs from magnetic resonance images using generative adversarial networks. *Med Phys*. 2018;45(8):3627-3636.
15. Navalpakkam BK, Braun H, Kuwert T, Quick HH. Magnetic resonance–based attenuation correction for PET/MR hybrid imaging using continuous valued attenuation maps. *Investig radiol*. 2013;48(5):323-332.
16. Krokos G, MacKewn J, Dunn J, Marsden P. A review of PET attenuation correction methods for PET-MR. *EJNMMI Physics*. 2023;10(1):52.
17. Mehranian A, Arabi H, Zaidi H. Vision 20/20: magnetic resonance imaging-guided attenuation correction in PET/MRI: challenges, solutions, and opportunities. *Med Phys*. 2016;43(3):1130-1155.
18. Catana C. Attenuation correction for human PET/MRI studies. *Phys Med Biol*. 2020;65(23):23TR02.
19. Alaskar H, Saba T. Machine learning and deep learning: a comparative review. *Proceedings of Integrated Intelligence Enable Networks and Computing: IIENC 2020*. 2021.143-150.
20. Castiglioni I, Rundo L, Codari M, et al. AI applications to medical images: from machine learning to deep learning. *Physica Med*. 2021;83:9-24.
21. Hatt M, Krizsan AK, Rahmim A, et al. Joint EANM/SNMMI guideline on radiomics in nuclear medicine: jointly supported by the EANM Physics Committee and the SNMMI Physics, Instrumentation and Data Sciences Council. *Eur J Nucl Med Mol Imaging*. 2023;50(2):352-375.
22. Stefano A. Challenges and limitations in applying radiomics to PET imaging: possible opportunities and avenues for research. *Comput Biol Med*. 2024;179:108827.
23. Weiger M, Pruessmann KP. Short-T2 MRI: principles and recent advances. *Prog Nucl Magn Reson Spectrosc*. 2019;114:237-270.
24. Ljungberg E, Damestani NL, Wood TC, et al. Silent zero TE MR neuroimaging: current state-of-the-art and future directions. *Prog Nucl Magn Reson Spectrosc*. 2021;123:73-93.
25. Grodzki DM, Jakob PM, Heismann B. Ultrashort echo time imaging using pointwise encoding time reduction with radial acquisition (PETRA). *Magn Reson Med*. 2012;67(2):510-518.
26. Froidevaux R, Weiger M, Brunner DO, Dietrich BE, Wilm BJ, Pruessmann KP. Filling the dead-time gap in zero echo time MRI: principles compared. *Magn Reson Med*. 2018;79(4):2036-2045.
27. Ahmadian S, Jabbari I, Bagherimofidi SM. Saligheh Rad H. Characterization of hardware-related spatial distortions for IR-PETRA pulse sequence using a brain specific phantom. *MAGMA*. 2021;34:213-228.
28. Khateri P, Saligheh Rad H, Jafari AH, et al. Generation of a four-class attenuation map for MRI-based attenuation correction of PET data in the head area using a novel combination of STE/Dixon-MRI and FCM clustering. *Mol Imaging Biol*. 2015;17:884-892.
29. Tustison NJ, Avants BB, Cook PA, et al. N4ITK: improved N3 bias correction. *IEEE Trans Med Imaging*. 2010;29(6):1310-1320.
30. Gupta SK, Pal R, Ahmad A, Melandsø F, Habib A. Image denoising in acoustic microscopy using block-matching and 4D filter. *Sci Rep*. 2023;13(1):13212.

31. van Griethuysen JJM, Fedorov A, Parmar C, et al. Computational radiomics system to decode the radiographic phenotype. *Cancer Res*. 2017;77(21):e104-e107.
32. Van Griethuysen JJ, Fedorov A, Parmar C, et al. Computational radiomics system to decode the radiographic phenotype. *Cancer Res*. 2017;77(21):e104-e107.
33. Dhal P, Azad C. A comprehensive survey on feature selection in the various fields of machine learning. *Applied Intelligence*. 2022;52(4):4543-4581.
34. Venkatesh B, Anuradha J. A review of feature selection and its methods. *Cybern Inf Technol*. 2019;19(1):3-26.
35. Chen T, Guestrin C. XGBoost: a Scalable Tree Boosting System. *Proceedings of the 22nd ACM SIGKDD International Conference on Knowledge Discovery and Data Mining*; 2016; San Francisco, California, USA.
36. Ke G, Meng Q, Finley T, et al. LightGBM: a highly efficient gradient boosting decision tree. *Proceedings of the 31st International Conference on Neural Information Processing Systems*; 2017; Long Beach, California, USA.
37. Vinayak RK, Gilad-Bachrach R. DART: Dropouts meet Multiple Additive Regression Trees. *ArXiv*. 2015;abs/1505.01866.
38. Abella M, Alessio AM, Mankoff DA, et al. Accuracy of CT-based attenuation correction in PET/CT bone imaging. *Phys Med Biol*. 2012;57:2477-2490.
39. Mackewn J, Stirling J, Jeljeli S, et al. Practical issues and limitations of brain attenuation correction on a simultaneous PET-MR scanner. *EJNMMI Phys*. 2020;7:1-17.
40. Liu X, Emami H, Nejad-Davarani SP et al. Performance of deep learning synthetic CTs for MR-only brain radiation therapy. *J Appl Clin Med Phys*. 2021;22(1):308-317.
41. Spadea MF, Pileggi G, Zaffino P, et al. Deep convolution neural network (DCNN) multiplane approach to synthetic CT generation from MR images—application in brain proton therapy. *Int J Radiat Oncol Biol Phys*. 2019;105(3):495-503.
42. Fu J, Singhrao K, Cao M, et al. Generation of abdominal synthetic CTs from 0.35 T MR images using generative adversarial networks for MR-only liver radiotherapy. *Biomed Phys Eng Express*. 2020;6(1):015033.
43. Spadea MF, Maspero M, Zaffino P, Seco J. Deep learning based synthetic-CT generation in radiotherapy and PET: a review. *Med Phys*. 2021;48(11):6537-6566.
44. Dovletov G, Pham DD, Pauli J, Gratz M, Quick HH. Improved MRI-based Pseudo-CT synthesis via segmentation guided attention networks. *InBIOIMAGING* 2022; pp. 131-140.
45. Kläser K, Varsavsky T, Markiewicz P, et al. Imitation learning for improved 3D PET/MR attenuation correction. *Med Image Anal*. 2021;71:102079.
46. Boukellouz W, Moussaoui A. Magnetic resonance-driven pseudo CT image using patch-based multi-modal feature extraction and ensemble learning with stacked generalisation. *J King Saud Univ*. 2021;33(8):999-1007.

How to cite this article: Hoseinipourasl A, Hossein-Zadeh G-A, Sheikhzadeh P, et al. Generation of synthetic CT from MRI for MRI-based attenuation correction of brain PET images using radiomics and machine learning. *Med Phys*. 2025;52:3772–3784. https://doi.org/10.1002/mp.17867